Spectrally-shaped illumination for improved optical monitoring of lateral III-V-semiconductor oxidation

Natan Monvoisin, Elizabeth Hemsley, Lucas Laplanche, Guilhem Almuneau, Stéphane Calvez, Antoine Monmayrant

Research Article Vol. 31, No. 8 / 10 Apr 2023 / Optics Express 12955
Optics EXPRESS

Spectrally-shaped illumination for improved optical inspection of lateral III-V-semiconductor oxidation

NATAN MONVOISIN, ELIZABETH HEMSLEY, LUCAS LAPLANCHE, GUILHEM ALMUNEAU, STÉPHANE CALVEZ, AND ANTOINE MONMAYRANT*

LAAS-CNRS, Université de Toulouse, CNRS, 7 Avenue du Colonel Roche, 31400 Toulouse, France
**antoine.monmayrant@laas.fr*

Abstract: We report an hyperspectral imaging microscopy system based on a spectrally-shaped illumination and its use to offer an enhanced in-situ inspection of a technological process that is critical in Vertical-Cavity Surface-Emitting Laser (VCSEL) manufacturing, the lateral III-V-semiconductor oxidation (AlOx). The implemented illumination source exploits a digital micromirror device (DMD) to arbitrarily tailor its emission spectrum. When combined to an imager, this source is shown to provide an additional ability to detect minute surface reflectance contrasts on any VCSEL or AlOx-based photonic structure and, in turn, to offer improved in-situ inspection of the oxide aperture shapes and dimensions down to the best-achievable optical resolution. The demonstrated technique is very versatile and could be readily extended to the real-time monitoring of oxidation or other semiconductor technological processes as soon as they rely on a real-time yet accurate measurement of spatio-spectral (reflectance) maps.

1. Introduction

Hyperspectral imaging is a technology that combines UV, visible and/or near infrared imaging with advanced spectroscopy techniques to offer spectrally- and spatially-resolved detection or monitoring. As such, it has emerged as an attractive and powerful inspection tool in an ever widening range of application areas including biology [1,2], pharmaceutics [3,4], defence and security [5], archeology and art conservation [6], food quality assessment [7], semiconductor material [8,9] and device metrology [10–12].

In the latter field, the capability to monitor the oxidation of (III-V) semiconductors has been proven to be a valuable tool especially for the fabrication of Vertical-Cavity Surface-Emitting Lasers (VCSELs) [13–15]. Indeed, these lasers, which have become the ubiquitous light sources for high-speed data transmission in datacenters and in LIDAR applications, rely on the selective oxidation of a thin buried semiconducting AlGaAs layer into an insulating oxide (AlOx), to define their electrical and optical aperture and, in turn, control their performance [16]. More specifically, since the geometric features of this lateral semiconductor/oxide aperture set the beam modal distribution, act on the modulation response bandwidth and may also be the source of dislocation defects causing device failure, in-situ real-time imaging of the oxidation process is a valuable asset to help reach and maintain high throughput high-yield VCSEL production. Technically and as illustrated below, this monitoring exploits the minute spectral changes in the VCSEL reflectivity between the oxidized and unoxidized regions to visualize the oxide aperture. To-date, the practical implementations have used a near-infrared camera illuminated with either a white-light broad spectrum or a single narrow-band spectrum [15]. In both cases, the aperture detection is challenging and of limited spatial resolution. Moreover it is highly dependant on the particular vertical stack of each VCSEL batch.

#480753 https://doi.org/10.1364/OE.480753
Journal © 2023 Received 11 Nov 2022; revised 10 Jan 2023; accepted 18 Jan 2023; published 5 Apr 2023

Optics EXPRESS

In this paper, we will present the methodology and the results of a versatile solution to shape the illumination spectrum for the application of in-situ imaging of the VCSEL oxide aperture. In particular, the proposed Spectrally-Shaped Source (S^3) enables weighting the spectral bands to accentuate low contrasts and increase the distinctness between regions of very close reflectivities. In addition, S^3 can be harnessed to acquire in-situ hyperspectral cube of the sample under study.

As focused in this paper, in the specific case of room temperature conditions and on an already oxidized VCSEL mesa, the distinctness of oxide aperture can be greatly improved by the use of the proposed spectrally-shaped illumination. With the future target of applying this optical method to high-temperature in-situ optical monitoring, this implementation of a static inspection could be transferred to dynamic tracking since reasonably short integration times are achievable and that the source can cover longer wavelengths to compensate the reflectance drift at high temperature.

2. Experimental setup

2.1. Spectrally-shaped source

The photograph of the spectrally-shaped source (S^3) is presented on fig. 1(a) together with a simplified diagram showing all the key components (fig. 1(b)). This type of system was first presented in [17–20]. The spectrum of a supercontinuum source is dispersed on a digital micromirror device (DMD), which selectively reflects desired wavelength bands into an optical fibre whose output end serves as the illumination source of the in-situ inspection system described in section 2.2 with a view to distinguish between two spatially contiguous areas where a buried AlGaAs layer has been oxidized or left as-grown.

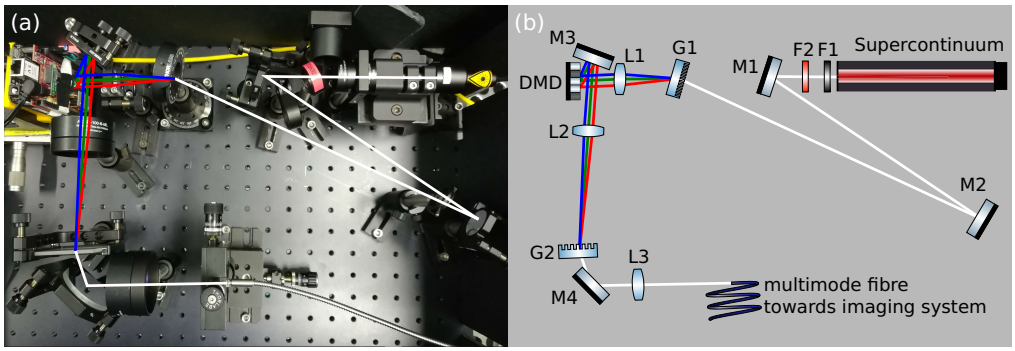

Fig. 1. Spectrally-Shaped Source: (a) photograph ; (b) schematic. Optical components : F1, F2 filters; M1..4 mirrors; G1, G2 gratings; L1..3 lenses; DMD digital micromirror device.

2.1.1. Optical system components

The supercontinuum light source has a [450-2400] nm spectral range whose fibered output is collimated to a beam diameter of ≃1 mm, and attenuated to eye-safe levels using a $OD = 1.7$ neutral density filter combination (`F1`).

As the spectral range of interest for in-situ monitoring of 850-nm-emitting VCSEL structures is in the NIR, the spectrum is then limited to [650-900] nm using a set of filters (`F2`). The beam is then dispersed by a 600-lines/mm transmission grating (`G1`) and focused on the DMD using a $f = 50$ mm cylindrical lens (`L1`).

The DMD used here is an 7.6-µm-pitch array of 640×360 square mirrors whose tilt axes lie along their diagonals. The DMD itself is tilted vertically by 8.73° so the reflected light remains on the horizontal plane. The light is spectrally dispersed along the full width of the DMD.

Optics EXPRESS

The light filtered by the DMD is collected using a $f = 100$ mm lens (L2) which has a large numerical aperture to capture the many diffraction orders emitted from the DMD [21–23] (see section D and fig. S4 of Supplement 1 for more details). Then the dispersed wavelengths are recombined using a second transmission grating (G2) with 300 lines/mm and coupled into a multimode fibre towards the in-situ monitoring setup (see fig. 3).

More details as well as the part numbers used in the setup can be found in section A of Supplement 1.

2.1.2. Spectral resolution and dispersion

The spectral resolution and dispersion of the S^3 is quantified by applying a black/white Heaviside step function mask across the 640 columns of the DMD, and fitting the measured transmission spectral response by a Gaussian error function (erf(.)). The fitted mean and standard deviation respectively gives the cutoff wavelength and the spectral resolution.

By scanning the step edge across the column number (labelled p), we are able to span the wavelength through the whole accessible spectral range.

The wavelength dispersion as a function of p is shown in fig. 2(a), while the resolution (*vs* p) is represented in fig. 2(b). The dispersion is seen to be strictly linear with a slope of $\Delta\lambda/\Delta p \simeq -0.24$ nm per DMD column, whereas the resolution is observed to be constant through the DMD columns at $\delta\lambda \simeq 0.89$ nm. Given the spatial spreading onto the DMD array, this resolution corresponds to $\simeq 3.7$ mirrors. Rounding up to 4 mirrors per band, the illumination is thus shaped into 160 independent bands over the full spectral range of $640 \times 0.24 \sim 153$ nm.

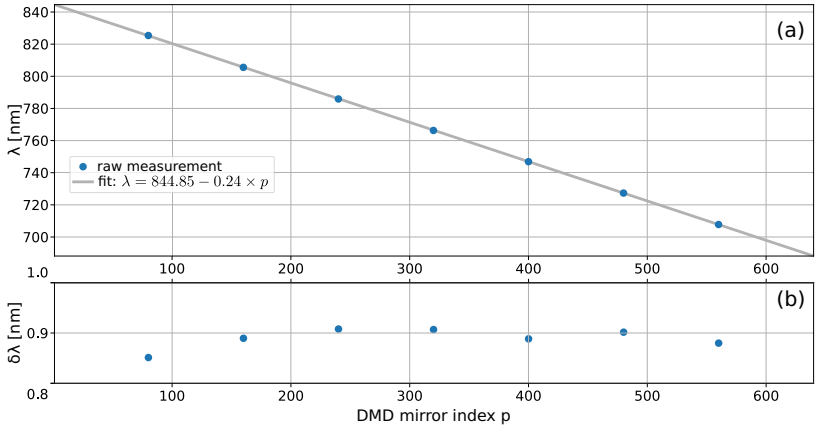

Fig. 2. Spectral calibration: (a) Wavelength and (b) spectral resolution as a function of the DMD mirror index p.

It is important to note that this spectral range can be tuned to match the spectral region of interest of the oxided-confined devices to be inspected. For instance, a simple rotation of the grating and change of the edge filters would allow the inspection of VCSELs operating at any near-infrared wavelength or of other oxidized vertical stacks. Moreover, for a larger spectral tuning, the hardware configuration could be easily modified (change of gratings and optics with different coatings). More details can be found in section E of Supplement 1.

2.1.3. Gray level calibration

The transmitted intensity per band is modified by adapting the [0-255] gray level of each DMD column using pulse width modulation (PWM). As the DMD we use here serves initially as a display for a system on chip (SOC) computer, it contains internal gamma correction curves,

Optics EXPRESS

leading to a non-linear relation between gray level and transmitted intensity that need to be taken into account for an accurate control of the transmitted spectrum. Details on this calibration can be found in section F of Supplement 1.

2.1.4. Shaped spectra

Arbitrary-shaped transmission spectra can be generated with a 0.9-nm resolution over a spectral range of ~ 153 nm, resulting in the ability to tailor the illumination spectrum as illustrated in fig. S11 of Supplement 1. Hereafter, we use this versatility to test for the most appropriate illumination spectrum which leads to the images with the highest distinguishability between the oxidized and unoxidized regions. As mentionned before, this shaped illumination spectrum can be easily and promptly tuned in accordance to the reflectivity contrast of the oxidized multilayer structure.

2.2. Lateral oxidation inspection system

The above-described spectrally-shaped source serves as the illumination source of the lateral oxidation inspection system schematically described on fig. 3.

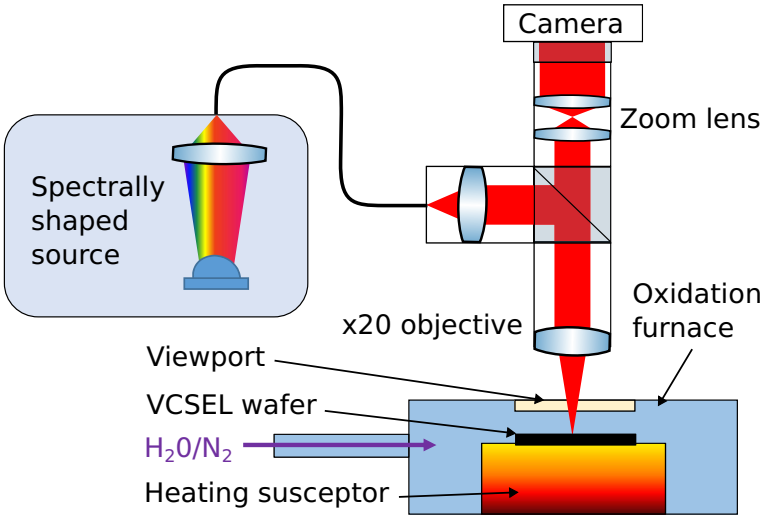

Fig. 3. Schematic of the oxidation furnace and in-situ monitoring system.

The latter is based on a long-working-distance microscopy setup that allows the acquisition of images of the surface of a particular VCSEL device whose buried AlGaAs layer is partially oxidized. Practically, a motorized micro-positioned microscope with a x20 objective (Mitutoyo G Plan APO), a x12 relay lens (Navitar ultra zoom) allows the recording of x17-magnification images using a VIS-NIR camera (Basler acA2000-165um). Coaxial illumination of the scene is obtained by relaying the output of the (≃ 1.5 mm-large-diameter 0.5-NA)-fibre-coupled light source described above.

Since the long-term intention in continuity with this work is to implement an in-situ, real-time monitoring of the lateral oxidation of III-V semiconductor devices, the observation setup, the source spectral coverage and the data acquisition and treatments were selected to be compatible with in-situ real-time tracking. In particular, the combined image acquisition and processing time was set to be 2 s, which will ensure the recording of successive oxide profiles with a <40 nm process-induced accuracy (the typical oxidation rate being ≃ 1 µm/min). However, all the measurements reported hereafter were carried out in static conditions i.e. for an already-oxidized

Optics EXPRESS

commercial VCSEL sample, with the VCSEL wafer maintained at room temperature and under inert atmosphere (no oxidizing water gas injection).

3. Results

3.1. Preliminary hyperspectral acquisition and illumination spectra setout

The determination of the relevant shaped spectrum requires the a-priori knowledge of the reflectivity spectra of both regions to distinguish, like the oxidized and unoxidized regions of the oxide aperture in a VCSEL. This data can be readily available (wafer from a known batch, data provided with the wafer,. . .) but can also be measured in-situ using S^3 as an hyperspectral imager.

The hyperspectral imaging could be performed using a classical wavelength scan, transmitting a single spectral band and recording each monochromatic image in a sequence. However, for high spectral resolution it requires very long integration times (as the illumination in each band is low) and can induce speckle distortion (as the coherence length is high). A more efficient approach is the Hadamard scan method [24], where each image corresponds to a linear combination of spectral bands, improving simultaneously upon both limitations. In particular, the gain in acquisition time between a wavelength scan and an Hadamard scan scales with the number of combined bands. In our current implementation of the Hadamard scan, we restrict ourselves to 127 5-column-wide bands and for each measurement in the scan, we combine 64 of these bands, resulting in a 64-fold improvement (see section H of Supplement 1 for more implementation details). This method also benefits from the Fellgett's advantage [24], that refers to a gain in the signal to noise ratio compared to the classical measurement. The Hadamard acquisition method requires however a data post-processing step that can be performed in a time and with a computational power compatible with future real-time oxidation monitoring.

The fig. 4(a) presents the image under panchromatic illumination of the VCSEL mesa, where the two regions to be detected are identified: the central dark area (and in particular the blue highlighted zone) corresponding to the non-oxidized part and the peripheral oxidized area (especially in orange donut). This image, as all the other images presented here, are recorded in-situ inside the oxidation furnace, at room temperature, from an already-oxidized VCSEL sample, and therefore can be defined as static acquisition.

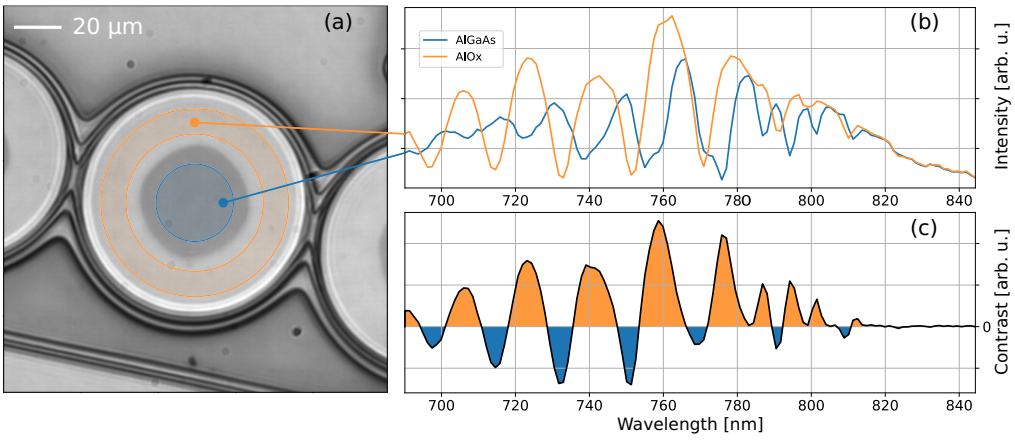

Fig. 4. (a) Top view of the sample under panchromatic illumination with AlOx (orange) and AlGaAs (blue) regions-of-interest, the etched mesa is delimited by three thin black lines outside of which is the bottom of the etch; (b) reflectivity spectrum in each region; (c) Spectrally-resolved reflectivity contrast between AlOx and AlGaAs regions.

Optics EXPRESS

From the hyperspectral cube measured using the Hadamard scan method, we extract the reflectivity spectra of both regions (see fig. 4(b)), from which we can determine the illumination spectral shape to increase the discernibility between regions. Considering this case with two different regions to discern, the Fisher discriminant analysis (FDA) can be efficiently applied [25]. The band weights to be applied are chosen to maximize the ratio of "inter-region variance" to "intra-region variance". As such, this method optimizes the separability by increasing the contrast between the two regions while minimizing the noise in each region. As a first step in this approach, we considered the noise to be constant across the spectral range and directly set the spectral band weights to the reflectivity contrast between the two regions (fig. 4(c)).

In order to simplify the acquisition and make it faster by applying a single mask, we chose only the positive part of the contrast distribution, which includes the highest cumulated contrast (filled orange curve in 4(c)).

In the remainder of this study, three different types of illumination are applied (panchromatic spectrum, monochromatic spectrum and shaped spectrum) as presented in fig. 5.

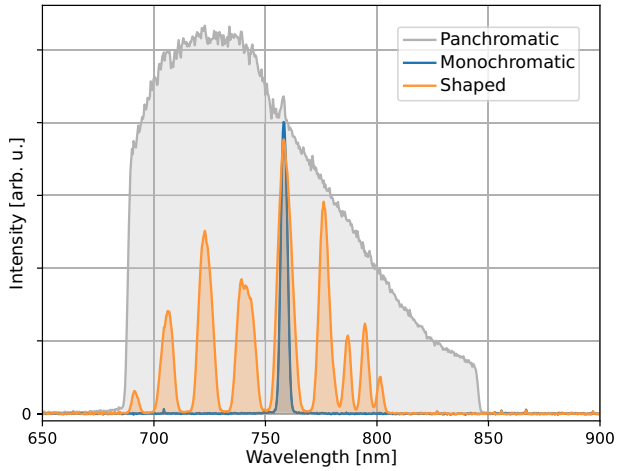

Fig. 5. The three illumination spectra generated with S^3: panchromatic spectrum (gray), monochromatic spectrum offering maximum contrast between AlOx and AlGaAs (blue), shaped spectrum (orange) corresponding to all the bands with positive contrast (see fig. 4(c)).

The panchromatic illumination (gray in fig. 5) consists in applying a fully white mask on the DMD. This corresponds to the supercontinuum source spectrum as transmitted by the S^3. The monochromatic illumination (blue in fig. 5) corresponds to the method used previously with lamp-source filtered through a monochromator. It is obtained by transmitting a 15-pixel-column-wide spectral band ($\simeq 3.75$ nm) centered at $\lambda = 758.66$ nm at which the contrast between AlOx and AlGaAs is maximum (see fig. 4(c)). The shaped illumination (orange in fig. 5) corresponds to the positive contrasts (see fig. 4(c)).

For each illumination, the integration time is tuned to take advantage of the full dynamic range of the camera resulting in 95 ms, 2000 ms and 400 ms respectively for the panchromatic, monochromatic and shaped illumination. In order to make a fair comparison despite the different acquisition times, acquired "views" are generated for each illumination as the sum of all the images acquired during a fixed time of $T = 2$ seconds, which, as already highlighted above, is fully compatible with the requirements of future real-time tracking.

Optics EXPRESS

3.2. Impact of the illumination on the monitoring views

The fig. 6 presents the impact of the illumination spectrum on the discernability of the AlGaAs and AlOx regions in the monitoring views. Three spectral illumination are considered: panchromatic (Figs. 6(a), 6(b)), monochromatic (Figs. 6(c), 6(d)), and shaped (Figs. 6(e), 6(f)) showing respectively the monitoring view and the corresponding histograms for the oxidized region (blue) and non-oxidized region (orange).

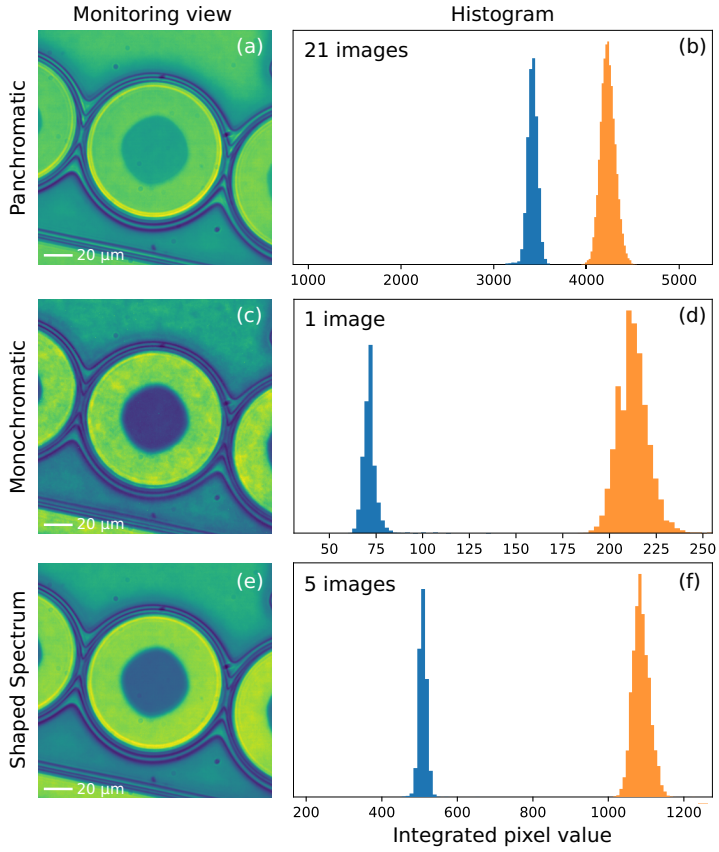

Fig. 6. [(a), (c), (e)] Monitoring views and [(b), (d), (f)] associated histograms in the oxidized (blue) and non-oxidized (orange) regions for three illumination spectra: [(a), (b)] panchromatic , [(c), (d)] monochromatic and [(e), (f)] shaped. A view corresponds to the sum of all the images acquired in $T = 2.0\,\mathrm{s}$.

The discernability between the two regions can be inferred by looking at the two peaks in the histograms of fig. 6: it increases both with increasing distance between the peaks and decreasing width of both peaks.

The resulting view with the panchromatic illumination corresponds to the sum of 21 images, each one acquired at an integration time of 95 ms. We see on fig. 6(a) and fig. 6(b) that this method gives a certain discernability between AlGaAs and AlOx regions, characterized by a relative low contrast and sharp peaks. For the monochromatic illumination case, corresponding to a single image with an integration time of 2 s, a better separation between the pixel mean value of each the regions is obtained. Albeit, on fig. 6(c), we observe the presence of grains, imputed to speckle patterns, inherent to the spectral coherence of the illumination. This can also

Optics EXPRESS

be seen in fig. 6(d) with the broadening of the histograms of both regions (speckle increasing the intra-region variance).

The view using the spectrally-shaped illumination, visible on fig. 6(e), is the sum of 5 images with an integration time of 400 ms. We see on its corresponding histogram, in fig. 6(f), that the spread of the pixel values of each regions has decreased compared to the monochromatic illumination, due to the disappearance of the speckle. Although the contrast with spectrally-shaped illumination is slightly smaller than with monochromatic illumination, as the intra-region variance is reduced (ie the peaks in the histogram are narrower), the discernability remains larger and results in better oxide edge detection as discussed hereafter.

3.3. Oxide edge detection

The last step to get the oxide aperture dimensions is the extraction of the contours from the monitoring views. This is performed all across the aperture circumference in steps of 2 degrees. At each step, we extract from the view a radial gray level curve, which starts at the mesa centre and extends across the oxidised region up to the mesa edge. This curve is then fitted with an erf(.) function whose mean value indicates the AlGaAs/AlO_x interface position.

The figs. 7(a), 7(b), and 7(c) show the view obtained during the inspection respectively for panchromatic, monochromatic and spectrally-shaped illuminations, with a magnified view on the AlGaAs/AlO_x interface respectively in figs. 7(d), 7(e), and 7(f). In all cases, the red curve corresponds to the detected oxide edge.

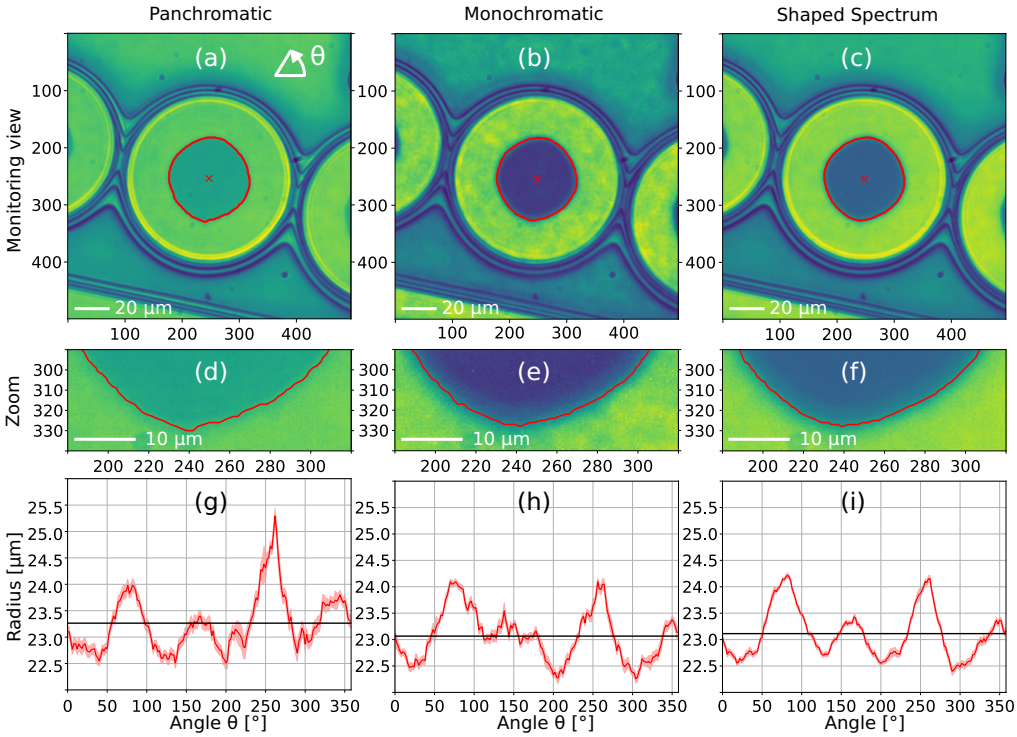

Fig. 7. Oxidation front measurements for three illumination spectra: panchromatic [(a), (d), (g)], monochromatic [(b), (e), (h)], shaped [(c), (f), (i)]. From the monitoring view [(a)-(c)] an error function fit is used to determine the position of the oxide front (red line), presented in polar coordinate in [(g)-(i)] together with the confidence interval of the fit (pink area) and the average radius (black line).

Optics EXPRESS

As one can see, for all three illuminations (see black lines in figs. 7(g), 7(h), and 7(i)), the average radius for the oxide aperture is similar, with values of 23.3, 23.1 and 23.1 µm for panchromatic, monochromatic and shaped illuminations respectively.

However, one can see that the fitted angular distributions are noticeably different. First, the confidence interval at 95 % of the fitted oxide radius (shown as a pink area in figs. 7(g), 7(h), and 7(i)), is reduced when going from panchromatic (127 nm) to monochromatic (90 nm) and to shaped-spectrum illumination (56 nm). This parameter quantifies the intrinsic uncertainty of the radius fitting and shows that the fit is the least noisy when illuminating with the shaped spectrum. In the latter case, the extracted oxide aperture angular distribution is observed to present four distinct maxima (at ~81, 167, 261 and 351 degrees) and four minima (at ~22, 130, 205 and 301 degrees) in agreement with the oxide aperture contour being a rounded diamond (squircle), as already observed in previous reports [26] and attributed to an anisotropic oxide progression [27]. For panchromatic and monochromatic illuminations, (figs. 7(g) and 7(h)) these peaks and valleys are harder to distinguish.

Last, because of the diffusive nature of the lateral wet oxidation [28], we expect a smooth profile for the oxide front. For panchromatic and monochromatic illuminations (figs. 7(g) and 7(h)), one can observe a high angular frequency component, whereas the profile is smoother, and thus more realistic, for shaped illumination (fig. 7(i)). This is a clear indication that shaped-spectrum illumination provides a better monitoring (Fig. 7(c)).

Additionally, it can also be noticed on Fig. 7(i) that the oxide aperture is a slightly deformed squircle (the radius at 81 and 261 degrees being longer than at 167 and 351 degrees), which may be due to the oxidation being impaired in the inter-mesa region (along the 167 and 351-degree direction) where the next mesas are in close proximity and the etching is not as deep. This kind of subtle observation is not achievable with panchromatic or monochromatic illuminations.

To further validate the above statements based on image analysis considerations and on oxidation physical insight, the above-studied VCSEL aperture (at the centre of Fig. 7(c)) was also imaged by Scanning Electron Microscopy (SEM). Given the aperture depth in the structure (>4 µm), a localized but destructive removal of the AlGaAs layers burying the oxide aperture by Focussed Ion Beam Etching (FIBE) had to be performed to be able to make this observation. Practically, as shown on Fig. 8(a), a ≃80-µm-diameter disk area was etched away from the 90-µm-diameter VCSEL mesa.

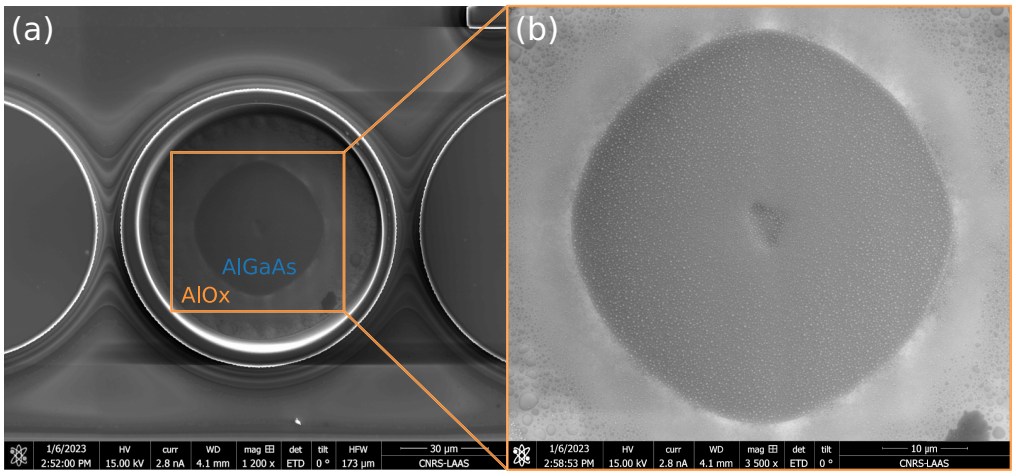

Fig. 8. Scanning Electron Microscope images of the AlOx aperture after Focussed Ion Beam Etching of the top layers: (a) overview of the circular aperture on the central mesa; (b) zoomed view of the aperture.

Optics EXPRESS

Figure 8(a) shows an overview image of the etched sample where the oxide aperture of the central VCSEL can easily be identified (as the boundary between the central dark grey unoxidised area and the surrounding light grey oxidized region) in contrast to the apertures of the off-centre VCSELs which are oxidized (see Fig. 7(c)) but were left unetched. Despite the FIBE artefacts (central etch dimple and <1-µm-diameter Gallium droplets lying on the etched surface), the zoomed SEM image of Fig. 8(b) clearly shows that the oxide aperture is indeed squircle-like and with a smooth profile as deduced from the optical image obtained under shaped-spectrum illumination.

Using (particle and mesa) features on the images, the composite image of Fig. 9, has been assembled based on Fig. 7(c), 8(a), 8(b) with the appropriate rescaling and rotation. As shown, the extracted aperture contour (dashed red line), obtained from the optical measurement on Fig. 7(c), closely matches the oxide aperture observed on the SEM image.

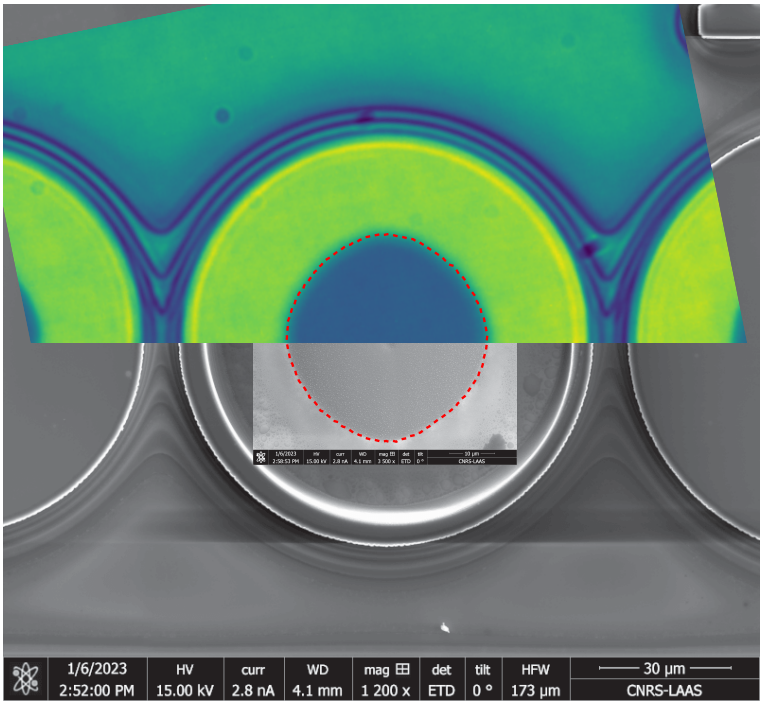

Fig. 9. Composite image with top to bottom overlap of the in-situ inspection view obtained with shaped spectrum illumination (clipped, with green colormap), the zoomed FIBE SEM image (light gray), the overview FIBE SEM image (darker gray). The dashed red line corresponds to the aperture fitted using the shaped spectrum illumination.

4. Conclusions

In this paper, a spectrally-shaped source based on a digital micromirror device has been set-up and used to provide a versatile illumination for in-situ inspection of the lateral wet oxidation process of III-V-semiconductor devices. This system has permitted images of oxide-apertured VCSELs to be recorded under conventional white-light (panchromatic), monochromatic, and a shaped-spectrum illumination tailored on purpose to correspond to the differences observed in the reflected spectra of the oxidized and unoxidized regions. Quantitative analysis of the quality of these images has revealed that the latter illumination scheme allows enhanced detection as a result of a compromise between the high-contrast but speckle-altered images of monochromatically-lit

Optics EXPRESS

scenes and the high-fluence (hence high-speed) recordings usually obtained using white light illumination. In addition, the same source has been used to acquire in-situ the whole hyperspectral cube of the sample under study. A subsequent SEM image on a single FIB-etched oxidized VCSEL has also been made and has enabled both qualitative and quantitative validations of the optical measurements.

The next step will be to implement this technique for real-time in-situ monitoring of the process, which implies taking into account the incidence of the real operating conditions on the aperture measurement such as high temperature environment, mechanical vibrations and other altering factors. Indeed, the discernability of the oxide aperture tends to fade at high temperature due to the increase of the optical absorption of the upper AlGaAs layers in the top Bragg mirror, and under these degraded conditions the parallel acquisition over multiple spectral bands will bring a significant gain to compensate for this lack of contrast.

The here-studied image recording system based on a spectrally-shaped source is amenable to implement more advanced image processing techniques such as the Fisher Discriminant Analysis, the Principal Component Analysis to further enhance the quality of the images and to subsequently lead to improved process monitoring and characterisation. The technique could also be used to improve the monitoring and control of other semiconductor processing steps where the distinguishability between side-by-side regions is key such as lithography and selective etching or deposition.

Funding. Agence Nationale de la Recherche (ANR-18-ASTR-0012-01, ANR-20-MERA-0002).

Acknowledgements. The fabrication process realized in this work was done within the LAAS-CNRS cleanroom facilities, member of the national *RENATECH* platform network. The authors thank Philipp Gerlach for his support.

Disclosures. The authors declare no conflicts of interest.

Data availability. Data underlying the results presented in this paper are available in Ref. [29].

Supplemental document. See Supplement 1 for supporting content.

References

1. L. Gao and R. T. Smith, "Optical hyperspectral imaging in microscopy and spectroscopy - a review of data acquisition," J. Biophotonics **8**(6), 441–456 (2015).
2. S. Ortega, M. Halicek, H. Fabelo, G. M. Callico, and B. Fei, "Hyperspectral and multispectral imaging in digital and computational pathology: a systematic review [invited]," Biomed. Opt. Express **11**(6), 3195 (2020).
3. L. M. Kandpal, J. Tewari, N. Gopinathan, P. Boulas, and B.-K. Cho, "In-process control assay of pharmaceutical microtablets using hyperspectral imaging coupled with multivariate analysis," Anal. Chem. **88**(22), 11055–11061 (2016).
4. X. Su, Y. Wang, J. Mao, Y. Chen, A. Yin, B. Zhao, H. Zhang, and M. Liu, "A review of pharmaceutical robot based on hyperspectral technology," J. Intell. & Robotic Syst. **105**(4), 75 (2022).
5. P. W. Yuen and M. Richardson, "An introduction to hyperspectral imaging and its application for security, surveillance and target acquisition," The Imaging Sci. J. **58**(5), 241–253 (2010).
6. H. Liang, "Advances in multispectral and hyperspectral imaging for archaeology and art conservation," Appl. Phys. A **106**(2), 309–323 (2012).
7. H. Pu, L. Lin, and D.-W. Sun, "Principles of hyperspectral microscope imaging techniques and their applications in food quality and safety detection: A review," Compr. Rev. Food Sci. Food Saf. **18**(4), 853–866 (2019).
8. X. Dong, A. K. Yetisen, J. Dong, K. Wang, P. Kienle, M. Jakobi, and A. W. Koch, "Hyperspectral fingerprints for atomic layer mapping of two-dimensional materials with single-layer accuracy," J. Phys. Chem. C **125**(30), 16583–16590 (2021).
9. F. Chouchane, G. Almuneau, O. Gauthier-Lafaye, A. Monmayrant, A. Arnoult, G. Lacoste, and C. Fontaine, "Observation of overstrain in the coalescence zone of AlAs/AlOx oxidation fronts," Appl. Phys. Lett. **98**(26), 261921 (2011).
10. B. Gawlik, C. Barrera, E. T. Yu, and S. V. Sreenivasan, "Hyperspectral imaging for high-throughput, spatially resolved spectroscopic scatterometry of silicon nanopillar arrays," Opt. Express **28**(10), 14209 (2020).
11. C. Yoon, G. Park, D. Han, S. il Im, S. Jo, J. Kim, W. Kim, C. Choi, and M. Lee, "Toward realization of high-throughput hyperspectral imaging technique for semiconductor device metrology," J. Micro/Nanopattern. Mats. Metro. **21**(02), 021209 (2022).
12. X. Buet, M. Zerrad, M. Lequime, G. Soriano, J.-J. Godeme, J. Fadili, and C. Amra, "Immediate and one-point roughness measurements using spectrally shaped light," Opt. Express **30**(10), 16078 (2022).

Optics EXPRESS

13. S. Feld, J. Loehr, R. Sherriff, J. Wiemeri, and R. Kaspi, "In situ optical monitoring of AlAs wet oxidation using a novel low-temperature low-pressure steam furnace design," IEEE Photonics Technol. Lett. **10**(2), 197–199 (1998).
14. A. Sakamoto, H. Nakayama, and T. Nakamura, "Fabrication control during AlAs oxidation of the VCSELs via optical probing technique of AlAs lateral oxidation (OPTALO)," in *SPIE Proceedings*, C. Lei and S. P. Kilcoyne, eds. (SPIE, 2002).
15. G. Almuneau, R. Bossuyt, P. Collière, L. Bouscayrol, M. Condé, I. Suarez, V. Bardinal, and C. Fontaine, "Real-time in situ monitoring of wet thermal oxidation for precise confinement in VCSELs," Semicond. Sci. Technol. **23**(10), 105021 (2008).
16. J. M. Dallesasse and D. G. Deppe, "III–V oxidation: Discoveries and applications in vertical-cavity surface-emitting lasers," Proc. IEEE **101**(10), 2234–2242 (2013).
17. T. C. Wood and D. S. Elson, "A tunable supercontinuum laser using a digital micromirror device," Meas. Sci. Technol. **23**(10), 105204 (2012).
18. Y. Gao, X. Chen, G. Chen, Z. Tan, Q. Chen, D. Dai, Q. Zhang, and C. Yu, "Programmable spectral filter in c-band based on digital micromirror device," Micromachines **10**(3), 163 (2019).
19. S. W. Brown, J. P. Rice, J. E. Neira, B. Johnson, and J. Jackson, "Spectrally tunable sources for advanced radiometric applications," J. Res. Natl. Inst. Stand. Technol. **111**(5), 401 (2006).
20. C.-H. Chuang and Y.-L. Lo, "Digital programmable light spectrum synthesis system using a digital micromirror device," Appl. Opt. **45**(32), 8308–8314 (2006).
21. X. Chen, B.-b. Yan, F.-j. Song, Y.-q. Wang, F. Xiao, and K. Alameh, "Diffraction of digital micromirror device gratings and its effect on properties of tunable fiber lasers," Appl. Opt. **51**(30), 7214–7220 (2012).
22. A. Sandmeyer, M. Lachetta, H. Sandmeyer, W. Hübner, T. Huser, and M. Müller, "DMD-based super-resolution structured illumination microscopy visualizes live cell dynamics at high speed and low cost," bioRxiv, 797670 (2019).
23. L. McMackin, M. A. Herman, and T. Weston, "Design of a multi-spectral imager built using the compressive sensing single-pixel camera architecture," in *Emerging Digital Micromirror Device Based Systems and Applications VIII*, vol. 9761 (International Society for Optics and Photonics, 2016), p. 97610G.
24. E. D. Nelson and M. L. Fredman, "Hadamard spectroscopy," J. Opt. Soc. Am. **60**(12), 1664 (1970).
25. R. A. Fisher, "The use of multiple measurements in taxonomic problems," Annals Eugen. **7**(2), 179–188 (1936).
26. G. Lafleur, G. Almuneau, A. Arnoult, H. Camon, and S. Calvez, "Modelling anisotropic lateral oxidation from circular mesas," Opt. Mater. Express **8**(7), 1788–1795 (2018).
27. S. Calvez, G. Lafleur, A. Arnoult, A. Monmayrant, H. Camon, and G. Almuneau, "Modelling anisotropic lateral oxidation from circular mesas," Opt. Mater. Express **8**(7), 1762–1773 (2018).
28. S. Calvez, P.-F. Calmon, A. Arnoult, O. Gauthier-Lafaye, C. Fontaine, and G. Almuneau, "Low-loss buried AlGaAs/AlOx waveguides using a quasi-planar process," Opt. Express **25**(16), 19275–19280 (2017).
29. N. Monvoisin, E. Hemsley, G. Almuneau, S. Calvez, and A. Monmayrant, "Spectrally Shaped Source," GitLab 2022, https://gitlab.laas.fr/nmonvoisin/scubed_project.